THE JOURNAL OF
PHYSICAL CHEMISTRY

Subscriber access provided by Univ. of Texas Libraries

Scanning tunneling microscopy and tunneling spectroscopy of n-type iron pyrite (n-FeS2) single crystals

Fu Ren Fan, and Allen J. Bard

J. Phys. Chem., **1991**, 95 (5), 1969-1976 • DOI: 10.1021/j100158a016

Downloaded from http://pubs.acs.org on January 26, 2009

More About This Article

The permalink http://dx.doi.org/10.1021/j100158a016 provides access to:

- Links to articles and content related to this article
- Copyright permission to reproduce figures and/or text from this article

ACS Publications
High quality. High impact.

The Journal of Physical Chemistry is published by the American Chemical Society.
1155 Sixteenth Street N.W., Washington, DC 20036

but the mechanism of the process is still not clearly understood. It has been speculated[8] that the reaction may be associated with vibrational relaxation that follows the intersystem crossing from S_1 to the triplet manifold or from T_1 into the vibrationally excited levels of the ground state. Tunneling between the vibrationless levels of the two tautomeric forms in the lowest excited singlet state was excluded, and the same conclusion had been reached earlier for the first triplet state.[38]

Another model proposed for the photoreaction observed in several porphine derivatives[39] assumes the transient formation of a "cis" tautomer (**2**), in which protons are located on adjacent nitrogen atoms. The energy of such a structure was postulated to be lower than that of a "normal" trans form in the T_1 state and higher in the S_0 state. Quite recently, the existence of a cis tautomer in the ground state was suggested by NMR.[40] Other hypothetical forms have also been proposed.[41]

We now summarize those observations made in rare gas matrices that promise to shed some light onto the mechanism of the reaction.

(i) The yields of photoinduced proton transfer from site A to B and from site B to A are the same within experimental error (10%). The relative efficiencies were measured by first transferring the population from one site into the other by laser irradiation and then monitoring changes in the visible absorption spectrum while simultaneously irradiating both sites. The latter was achieved by using the light source of the FT spectrophotometer, which simultaneously was recording the absorption.

(ii) We observed an isotope effect on the proton-transfer efficiency in **1**-d_2 vs **1**-d_0. The photoinduced reaction was roughly an order of magnitude slower in the deuterated compound.

(iii) The tautomerization yield in Xe and Kr matrices was practically temperature independent in the range 10-40 K. At higher temperatures, the reaction yield increased considerably.

(iv) Photoinduced double proton transfer is slower in the heavier inert gas matrices. This was found upon observing how long the sample photooriented by irradiation with polarized light remained dichroic while being exposed to the analyzing light of the instrument. The LD signal decreased much faster in Ar than in Xe matrices. It should be noted that, at the temperatures used, the rate of the dark ground-state reaction is completely negligible.

(v) Single-site fluorescence and phosphorescence spectra were obtained from both dominant sites, A and B.

The fact that single-site emissions are observed is difficult to reconcile with a model of reaction occurring on the excited-state energy surface with only two minima, since in this case one would expect to see emissions from both sites even after selective excitation of only one site, unless the efficiency of the process is very weak. On similar grounds, "hot" triplet state reaction also seems improbable.

Although our results clearly cannot be said to "prove" any mechanism, they are perfectly compatible with a model of tautomerization occurring in the lowest triplet state and involving a third, lower energy minimum, most probably corresponding to the cis tautomeric structure (**2**).[39] The molecule would move into this minimum in a rate-determining step by proton tunneling and at higher temperatures also by barrier crossing; see (iii) above. Fast intersystem crossing to the ground state of the cis form would then occur, promoted by the presumably lower T_1-S_0 gap in **2**, followed by return to the trans species of either the substrate or product. In this model, the efficiency of the tautomerization process should be directly proportional to the triplet lifetime, and thus higher in the lighter inert gas matrices, exactly as observed.

A definitive proof of such a scheme would be the direct observation of the cis triplet intermediate **2** in absorption or emission. The difficulty is that such a species is most probably extremely short-lived. Its presence might well be obscured in absorption by much higher populations of the triplet state of the usual trans isomer **1**. The phosphorescence quantum yield of the cis form might well be very small and the wavelength very inconvenient for sensitive detection.

The above observation (iii) provides a hint against the hot S_0 state mechanism, since the rate of vibrational cooling of a hot porphine molecule in the matrix should not be temperature-independent.

We are currently continuing our mechanistic investigation; preliminary results indicate that direct irradiation into the origin of the $T_1 \leftarrow S_0$ transition to the lowest triplet state of site A produces a slow change in the relative site population. By avoiding the S_1 state, this would prove that the tautomerization is capable of proceeding on the T_1 or the S_0 surface.

Acknowledgment. This work was supported by grants from the National Science Foundation (CHE9000292) and the National Institutes of Health (GM 37929).

(38) Van Dorp, W. G.; Schoemaker, W. M.; Soma, M.; van der Waals, J. H. *Mol. Phys.* **1975**, *30*, 1701.
(39) Dvornikov, S. S.; Kuz'mitskii, V. A.; Knyukshto, V. N.; Solov'ev, K. N. *Dokl. Akad. Nauk SSSR* **1985**, *282*, 362.
(40) Schlabach, M.; Rumpel, H.; Limbach, H.-H. *Angew. Chem., Int. Ed. Engl.* **1989**, *28*, 76.
(41) Bersuker, G. I.; Polinger, V. Z. *Chem. Phys.* **1984**, *86*, 57.

Scanning Tunneling Microscopy and Tunneling Spectroscopy of n-Type Iron Pyrite (n-FeS_2) Single Crystals

Fu-Ren Fan and Allen J. Bard*

Department of Chemistry, The University of Texas at Austin, Austin, Texas 78712 *(Received: June 15, 1990; In Final Form: August 21, 1990)*

The (001) surface of a highly doped (>2.7 × 10^{18} cm^{-3}) n-type FeS_2 crystal was imaged by the constant current mode in air with a scanning tunneling microscope (STM). Current (*i*) images at different bias voltages (*V*) were also obtained. Tunneling spectroscopy (TS) was carried out, and *i* vs *V* and d*i*/d*V* vs *V* curves obtained with the tip held above the FeS_2 surface were interpreted in terms of the band locations and a localized state within the band gap. The effect of band bending in the semiconductor on the interpretation of the TS results is also considered.

Introduction

In this paper we present the results of scanning tunneling microscopy (STM) and related tunneling spectroscopy (TS) and scanning tunneling spectroscopy (STS) studies on the transition-metal dichalcogenide n-FeS_2. Transition-metal dichalcogenides have been shown to be promising semiconductors for electrochemical regenerative and photoelectrolysis cells.[1] Its stability against anodic photocorrosion has been attributed to

(1) Tributsch, H. *Struct. Bonding* **1982**, *49*, 127.

0022-3654/91/2095-1969$02.50/0 © 1991 American Chemical Society

photoinduced hole transfer via transition-metal d states. While information about the electronic structures of clean surfaces can be obtained by ultrahigh vacuum (UHV) techniques, such as photoemission spectroscopy [UPS, XPS, inverse photoemission (IPS)], the exact distribution of the surface electronic states involved in actual electron-transfer processes is still unknown and is more suitably determined by an in situ technique for samples exposed to gaseous or liquid environments.

There have recently been several reports concerning studies of semiconductor surfaces by STM and TS in gaseous or liquid environments. Gilbert and Kennedy[2] investigated the electronic structures of n-TiO_2 (001) and α-Fe_2O_3 (0001) single-crystal surfaces and the effect of surface treatment on topography. Itaya and Tomita[3] studied the semiconductor/aqueous solution interface and the effect of substrate potential on the STM behavior. Sakamaki et al.[4] investigated the surface density of states (SDOS) of hydroxylated and reduced n-TiO_2 (110) single crystals and showed that the SDOS are different from the states in the bulk material. Kaiser et al.[5] investigated H-terminated silicon surfaces in a dry nitrogen atmosphere. We have recently studied an n-type TiO_2 (001) surface and examined its surface electronic states.[6] We continue in this work with STM, TS, and STS studies on n-FeS_2.

Experimental Section

The highly conductive n-type iron pyrite, n-FeS_2, single-crystal samples (resistivity $\lesssim 0.01\ \Omega$ cm, ca 2.5 mm × 2.5 mm × 2.5 mm) were generously donated by Professor H. Tributsch. The doping density was calculated from the resistivity and the known electron mobility in FeS_2 (230 $cm^2\ s^{-1}\ V^{-1}$).[12a] Most samples were used without further treatment, but were cleaned in methylene chloride and then methanol followed by rinsing with Millipore reagent water before mounting on the sample holder. Ohmic contacts were made by rubbing In–Ga alloy on one side of the sample cube. The surface studied was the (001) surface.

The STM apparatus and the detailed procedures for conductance measurements have been described previously.[6] Briefly, current images (constant height) were obtained by first stabilizing the feedback loop at a reference voltage of −0.2 V and reference current of 0.5 nA and then interrupting the feedback loop and measuring the tip current at the desired bias (sample vs tip), e.g., +0.2 or −1.0 V, at each location. In tunneling spectroscopy measurements, after interruption of the feedback loop, the voltage between sample and tip (V) was swept linearly at ca. 2 V/s and the current (i) recorded to obtain the i–V curve. A 10–20-mV peak-to-peak sinusoidal signal (ΔV) at 10 kHz was superimposed on the dc ramp and the variation in the in-phase current (Δi) was determined with a lock-in amplifier to obtain the conductance, di/dV as a function of V. Typically 10–50 scans, collected over a period of a few minutes, were averaged and the tunneling spectra, (di/dV) or $(di/dV)/(i/V)$ vs V were plotted.

Electrochemically etched Ir-Pt (FHC Co., Brunswick, ME) tips were employed. The current and conductance measurements were performed with relatively blunt tips and thus represent a spatial average over an area that was larger than a surface unit cell; however, sharper tips were used for the STM imaging. All experiments were performed in air and in the dark.

Results

STM Images. In Figure 1A we show a typical 128 nm × 128 nm constant-current topographic image of the n-FeS_2 (001) surface acquired at a voltage (substrate vs tip) of −0.2 V and a reference current of 0.5 nA. The overall morphology of the surface is rough; however, it is still easy to find fairly large atomically flat regions (mesas) covering several hundreds of angstroms (see the lower left corner of Figure 1A). As shown in this figure near one of the diagonals, we observe a few dislocation bands, perhaps belonging to the slip systems along the easy-glide direction (001). We occasionally observed this type of dislocation within the areas imaged. In Figure 1C,D, we show two current images acquired simultaneously with the topograph (Figure 1A) but with bias voltages of −1.0 (Figure 1C) and 0.2 V (Figure 1D). The difference between these two current images reflects mainly the spatial distribution of the surface electronic states rather than geometric structures (surface topography). As described in the Experimental Section, these images were obtained by first biasing the substrate vs tip to −0.2 V and 0.5 nA and then interrupting the feedback loop and measuring the current at the desired bias. Note that a current image taken with the same procedure at the same voltage as the constant-current topograph (−0.2 V, Figure 1B) shows no structure even at a magnification 50 times that of the current scale shown in Figure 1C,D. The current image obtained at large negative bias voltage, Figure 1C, shows stronger current signals in the regions where the topograph is fairly smooth (see the lower left corners of Figure 1A,C). The positive-bias current image, Figure 1D, shows larger currents in the regions where the slip dislocations are abundant (see, for example, the lower right corners of Figure 1A,D). These images show distinct bias-dependent structures that are perhaps derived from electron transfer through different electronic states of the semiconductor and might represent the chemical heterogeneity of the surface. However, these states are not correlated with the monatomic step edges between the smooth mesas and for the negative bias region, even for the more pronounced surface features. To identify the energies of these states, we examined the current–voltage (i–V) and conductance–voltage (di/dV–V) characteristics of the substrate surface as described in the following sections.

Iron pyrite has a cubic structure formed by an fcc lattice of Fe atoms and by S–S "dumbbells" located in the middle of the edges and in the center of the cubic cell, with the S–S dumbbells lying along the four nonintersecting (111) directions. Hence the projection of the pyrite structure on the (001) plane exhibits a nonsmooth or "wavy" profile as shown in Figure 2A. In Figure 2C,D we show two higher resolution current images acquired simultaneously with voltages of −0.5 (Figure 2C) and 0.5 V (Figure 2D) at a rastering rate of ca. 0.2 Hz. Wavy atomic ridges (shown as broken zigzag lines in Figure 2A,C,D) with a spacing of ca. 2.7 Å are clearly seen; however, neither iron nor sulfur atoms are clearly resolved in both images, although the positive-bias current image, Figure 2C, exhibits a greater current protrusion. In Figure 2B we show a current image obtained at a higher negative bias voltage (−1.0 V) and at a higher rastering rate (ca. 2 Hz). The fcc structures formed by the Fe atoms are more clearly observed. These distinct bias-dependent current images are derived from electron transfer from different states of the semiconductors and the tip. They have been clearly observed in UHV STM studies of Si[7,8] and GaAs[9] but have not been reported for gaseous and liquid environments where the environment can affect the surface energy levels.

Current–Voltage and Current–Distance Relations. In Figure 3 the experimentally determined i–V relationships for highly conductive iron pyrite single-crystal samples (doping density >2.7 × 10^{18} cm^{-3}) at various tip–samples separations, s, are shown. The separation at a designated current and bias voltage (i = 0.5 nA at V = −1.0 V) was arbitrarily taken as the reference gap, s_0 (curve 1), with relations at smaller gaps shown in curves 2–4. As shown in Figure 3, the i–V behavior at a given s is linearly dependent on V at small bias voltages and approaches a nearly exponential dependence at larger bias. Moreover, unlike the n-TiO_2 crystal

(2) See, e.g.: (a) Gilbert, S. E.; Kennedy, J. H. *J. Electrochem. Soc.* **1988**, *135*, 2385. (b) Gilbert, S. E.; Kennedy, J. H. *Langmuir* **1989**, *5*, 1412.
(3) See, e.g.: (a) Itaya, K.; Tomita, E. *Chem. Lett.* **1989**, 285. (b) Itaya, K.; Tomita, E. *Surf. Sci.* **1989**, *219*, L515.
(4) Sakamaki, K.; Itoh, K.; Fujishima, A.; Gohshi, Y. *J. Vac. Sci. Technol. A* **1990**, *8*, 614.
(5) Kaiser, W. J.; Bell, L. D.; Hecht, M. H.; Grunthaner, F. J. *J. Vac. Sci. Technol. A* **1988**, *6*, 519.
(6) Fan, F.-R.; Bard, A. J. *J. Phys. Chem.* **1990**, *94*, 3761.
(7) Hamers, R. J.; Tromp, R. M.; Demuth, J. E. *Phys. Rev. Lett.* **1986**, *56*, 1972.
(8) Feenstra, R. M.; Stroscio, J. A.; Fein, A. P. *Surf. Sci.* **1987**, *181*, 295.
(9) Feenstra, R. M.; Stroscio, J. A.; Tersoff, J.; Fein, A. P. *Phys. Rev. Lett.* **1987**, *58*, 1192.

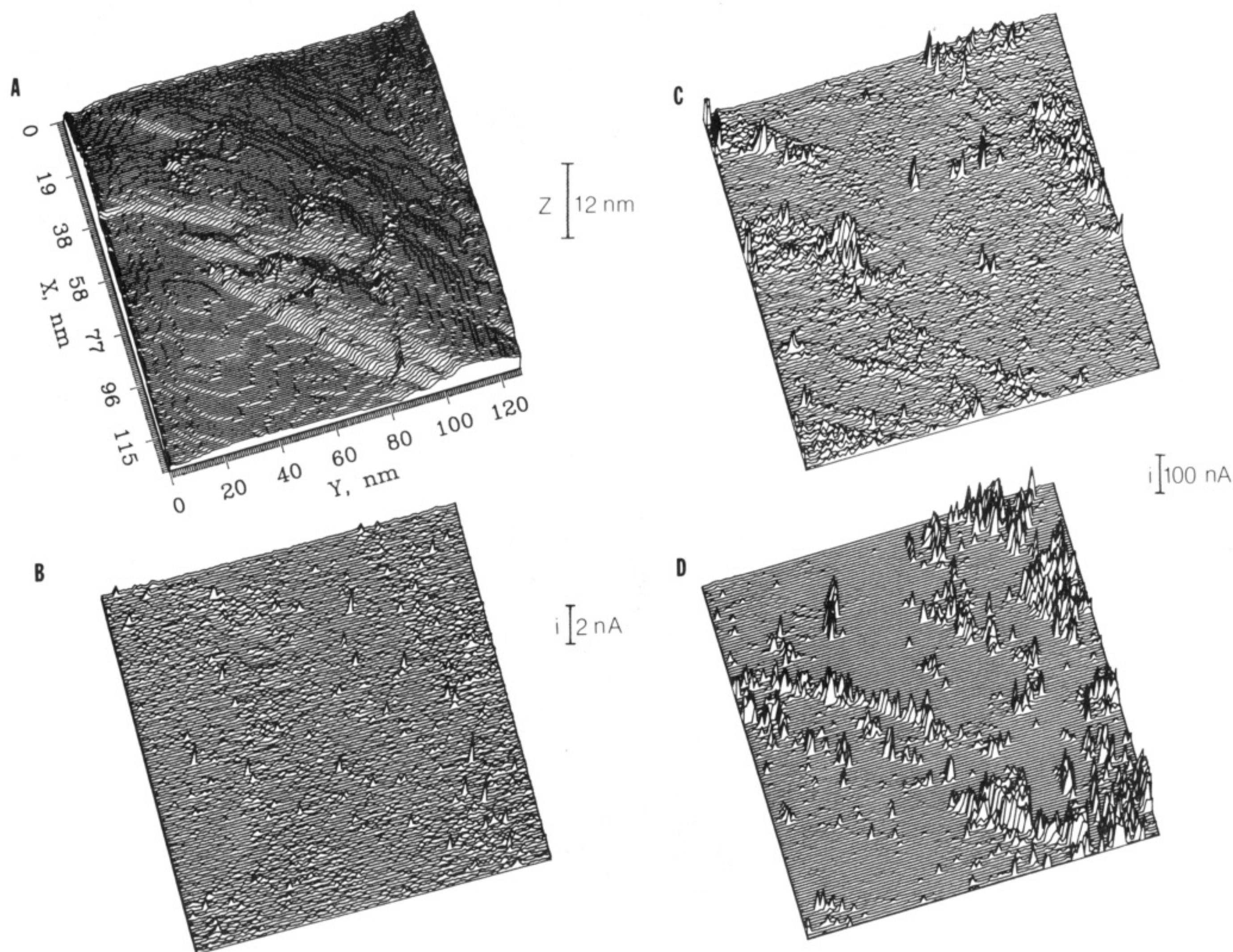

Figure 1. (A) Typical 128 nm × 128 nm constant-current topographic image of the n-FeS_2 (001) surface, acquired at a sample voltage of −0.2 V and a reference current of 0.5 nA. The rastering rate of the tip was ca. 5 s/line. The maximum height is ca. 60 Å. (B) Current image acquired at a sample voltage of −0.2 V after stabilizing the feedback loop at a voltage of −0.2 V and a reference current of 0.5 nA and then interrupting the feedback loop. The current scale has been magnified 50 times as compared with that for Figure 1C,D. (C) Current image acquired at −1.0 V after 1B. (D) Current image acquired at 0.2 V after 1C.

reported previously,[6] the i–V curves of these iron pyrite samples display only slight rectifying behavior, behaving rather as degenerate metal/insulator/semiconductor (MIS) junctions.[10] This behavior might be due to the high conductivity of the pyrite samples studied. Note that for a given voltage the current is larger at positive bias (tip negative) than at negative bias, opposite to what is predicted for a Schottky barrier with an n-type semiconductor. As shown in Figure 3, the magnitude of the current at a given bias is strongly dependent on s. We performed an independent series of experiments by measuring the current as a function of the change in s at various negative bias voltages. Two typical curves are shown in Figure 4; the experimental curves for other bias voltages fell between these two lines. As shown, i is essentially exponentially dependent on s, i.e., the i–s curves behave as

$$i \propto \exp(-\kappa s) \quad (1)$$

Within experimental uncertainty, κ was essentially independent of the voltage in the range from −0.25 to −1.5 V and had an average value of ca. 1.5 $Å^{-1}$. If we assume i is tunneling limited, κ is given by eq 2,[11] where m is the electron mass, h is Planck's constant, and ϕ is the effective barrier height. We obtain an estimated effective barrier height for tunneling of only 2.2 eV, which is much smaller than the reported work functions of most metals and semiconductors.

$$\kappa = (4\pi/h)(2m\phi)^{1/2} \quad (2)$$

Conductance–Voltage Measurement. Figure 5 shows a typical conductance (di/dV) spectrum for a heavily-doped (ca. 2.7×10^{18} cm^{-3} doping density) n-FeS_2 single-crystal sample over the bias voltage range of −1.8 to +1.8 V. This spectrum is the conductance spectrum taken at s_0 averaged with that at $s_0 - 2.5$ Å, in the bias voltage region where the two spectra overlap. The spectra have been corrected for the distance dependence by dividing di/dV values by $e^{-\kappa s}$ ($\kappa = 1.5$ $Å^{-1}$). Note that as with the n-TiO_2 (001) surface reported previously,[6] there is a wide region of low conductance referred to as the "conductance well", terminating at both ends in regions of sharply rising conductance. This conductance well becomes more pronounced after normalizing the differential conductance (di/dV) with the integral conductance (i/V) to remove the large increase of di/dV with voltage, which tends to mask the smaller features in the conductance spectrum. The conductance well has a width close to that of the indirect band gap of FeS_2 (ca. 0.95 eV,[12] see Figure 6). Also shown in Figure

(10) Sze, S. M. *Physics of Semiconductor Devices*; Wiley: New York, 1981; Chapters 7 and 9.

(11) See, e.g.: (a) Hansma, P. K.; Tersoff, J. *J. Appl. Phys.* **1987**, *61*, R1. (b) Kuk, Y.; Silverman, P. J. *Rev. Sci. Instrum.* **1989**, *60*, 165.

(12) (a) Ennaoui, A.; Fiechter, S.; Goslowsky, H.; Tributsch, H. *J. Electrochem. Soc.* **1985**, *132*, 1579. (b) Schlegel, A.; Wachter, P. *J. Phys. C* **1976**, *9*, 3363.

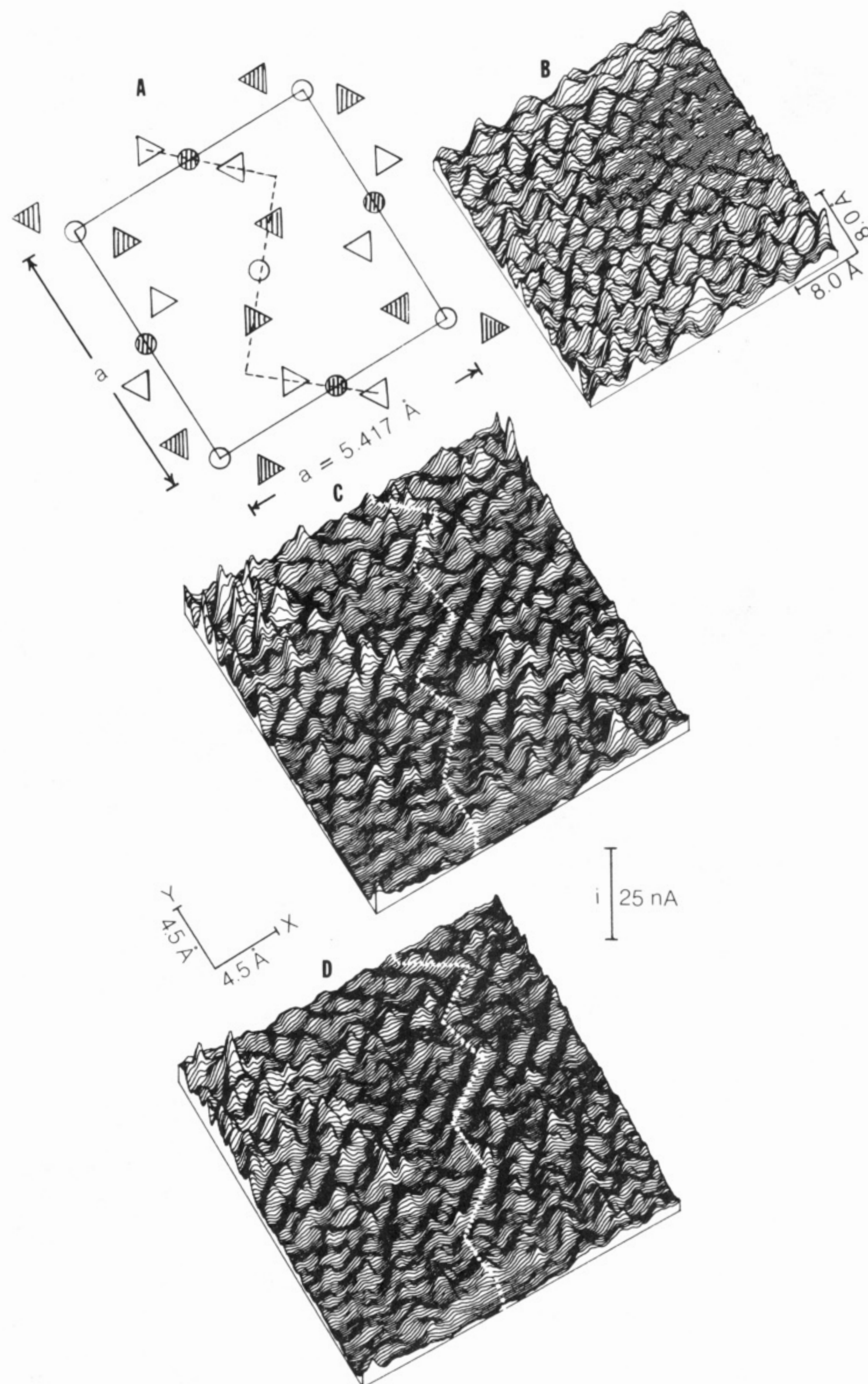

Figure 2. (A) Projection of the iron pyrite structure on the (001) plane, showing a "wavy" or "zigzag" profile. Fe atoms: ○, 0; ⊘, a/2. S atoms: △, −0.115a; ▽, 0.115a; ▲, 0.385a; ▼, 0.615a. a = 5.417 Å. (B) High-resolution current image acquired at a sample voltage of −1.0 V at a rastering rate of ca. 2 Hz. The current corrugation amplitude is in the range 1.4–11.7 nA. C and D are two current images acquired simultaneously with voltages of −0.5 (C) and 0.5 V (D) at a rastering rate of ca. 0.2 Hz. The current corrugation amplitude is in the range of 0.6–17.5 nA for (C) and 0.8–17.2 nA for (D). The wavy atomic ridges are shown as broken zigzag lines in A, C, and D.

6, the normalized conductance spectrum, in the positive bias region is a broad peak of width ca. 1.5 eV, with several fine features superimposed. In the negative-bias region, the conductance spectrum shows a narrow peak ($\gtrsim$0.5 eV wide) centered around ca. −1.6 V, which is superimposed on a high increasing background. Also shown in Figure 6 is a small, but distinct, peak located at ca. −0.25 V, which we tentatively attribute to an impurity state associated with an electron donor. One may be able to identify this state by investigating crystals with different doping densities.

Discussion

In this section we apply a similar scheme as that used to explain our n-TiO_2 results[6] to interpret the experimental work presented in this paper. In addition, we analyze the potential distribution

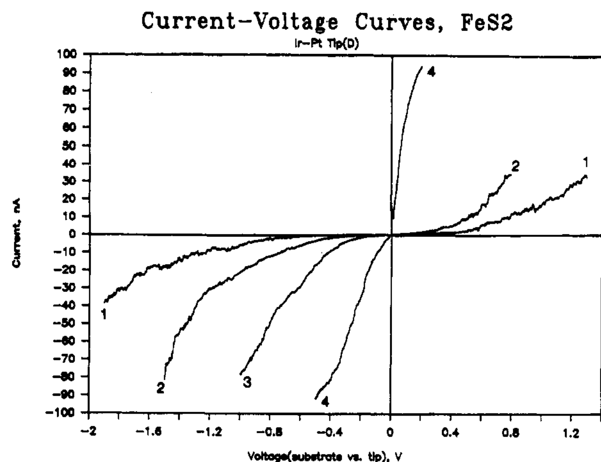

Figure 3. Current vs voltage curves for an Ir-Pt tip and n-FeS_2 sample at various tip-sample separations. 1: reference tip-sample separation (s_0) defined by a current 0.5 nA at bias voltage −1.0 V. 2: s_0 −2.5 Å. 3: s_0 −5.0 Å. 4: s_0 −10 Å.

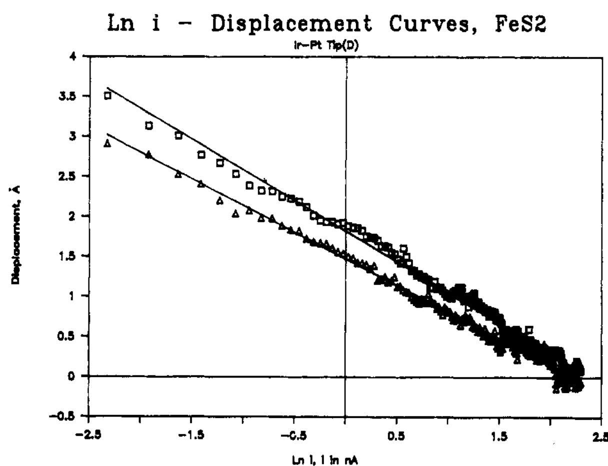

Figure 4. ln (current) vs vertical tip displacement at bias voltages −0.25 (squares) and −1.0 V (triangles).

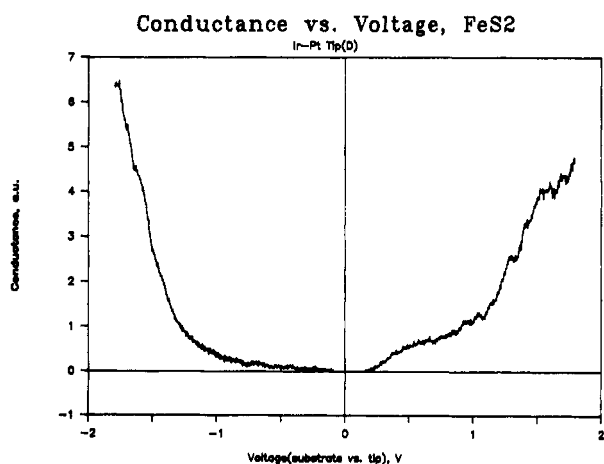

Figure 5. Conductance (di/dV) as a function of voltage for an Ir-Pt tip and n-FeS_2 sample. Modulation frequency of 10 kHz and modulation amplitude of 20 mV peak-to-peak were employed in the phase-sensitive technique.

in the insulator tip-substrate gap as a function of applied voltage based on a simplified one-dimensional MIS tunnel structure. Figure 7A shows an ideal n-type MIS tunnel structure with flat energy bands and with no applied bias voltage. For simplicity, we assume that tip and semiconductor have the same work function (i.e., initially $E_{FM} = E_{FS}$). Without including the contribution from surface states, there are four possible current components associated with the conduction and valence bands of the semi-

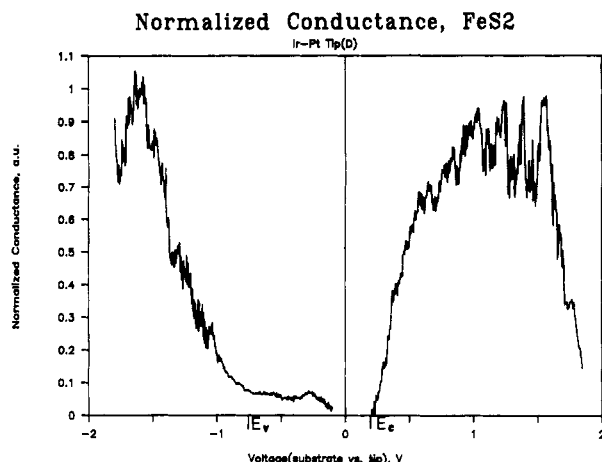

Figure 6. Normalized conductance $(di/dV)/(i/V)$ as a function of bias voltage. Same experimental conditions as in Figure 5 were used.

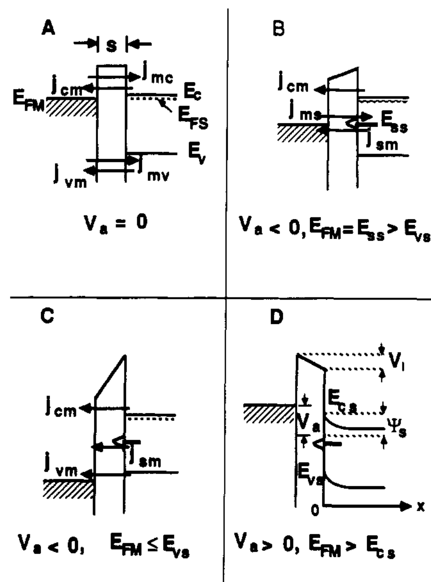

Figure 7. (A) Energy band diagram of an ideal n-type MIS structure defining the four current components via the energy bands of the semiconductor (see the descriptions in the text). B–D are the energy band diagrams for n-type MIS structures showing potential distribution under different bias conditions. E_{FM} is the Fermi level in the bulk of the metal; E_{FS} is the Fermi level of the semiconductor in the bulk; E_c and E_v are the CB and VB edges of the semiconductor in the bulk; E_{cs} and E_{vs} are the corresponding values at the surface. E_{ss} is the surface state energy; V_a is the applied voltage; V_i is the voltage drop across the insulator, and ψ_s is the semiconductor surface potential.

conductor. They are electron flows from the metal to the conduction band (CB) of the semiconductor (j_{mc}), from the CB of the semiconductor to the metal (j_{cm}), from the metal to the valence band (VB) of the semiconductor (j_{mv}), and from the VB of the semiconductor to the metal (j_{vm}). Each differential current density at bias voltage V produced by states at energy E, $dj_{\mu\nu}$, can be represented by a general expression

$$dj_{\mu\nu} = qk_{\mu\nu}(E,V,s)\ \rho_{\mu o}(E,V)\ \rho_{\nu u}(E,V)\ dE \qquad (3)$$

where different subscripts μ, ν represent the different current components (i.e., when $\mu = m$, $\nu = c$ or v, and vice versa), q is the charge of the electron, $k_{\mu\nu}(E,V,s)$ is the distance-dependent rate constant for electron transfer from μ to ν at a bias voltage V for a state at energy E at distance s. $\rho_{\mu o}(E,V)$ and $\rho_{\nu u}(E,V)$ are the occupied density of states in μ and the unoccupied density of states in ν for states at energy, E, and bias voltage, V, respectively. Assuming an ideal metal with a constant density of states, we approximate the diffential conductivity as[13]

$$dj_{\mu\nu}/dV \propto k_{\mu\nu}(E,V,s)\ \rho_s(E,V) \qquad (4)$$

where $\rho_s(E,V)$ is the density of states of the semiconductor evaluated at the metal position at energy E and bias voltage V. In this paper we do not intend to evaluate eqs 3 and 4 explicitly but rather to use them as qualitative guidelines to explain the experimental results.

As implied by eqs 3 and 4, when a negative bias is applied to the semiconductor, the Fermi level in the metal (E_{FM}) moves below that in the bulk of the semiconductor (E_{FS}, Figure 7B). j_{mc} will be small, because only those electrons in the metal with energies greater than the CB edge of the semiconductor at the surface (E_{cs}) will be able to transfer to the CB of the semiconductor. j_{mc} is expected to decrease with increasing negative bias voltage. However, j_{cm} will increase slightly with increasing negative bias, since the electrons in the CB of the semiconductor see more empty states in the metal. The slowly increasing conductance observed in the low negative-bias voltage region (e.g., between 0 and −1.0 V), as shown in Figure 5, mainly represents contributions from this component. Both j_{mv} and j_{vm} are small compared to j_{mc} and j_{cm} at low negative-bias voltage, since there are essentially no available empty states in the metal or in the semiconductor VB for electron transfer. However, with an increase in the negative bias voltage (e.g., ≤−1.0 V for the present case), E_{FM} drops below the VB edge at the semiconductor surface (E_{vs}, see Figure 7C). Now, j_{vm} can be large because the electrons in the VB of the semiconductor have a large number of empty states in the metal available. The sharp increase of the conductance observed at high negative bias voltages (<−1.0 V), as shown in Figure 5, is mainly attributed to this component. However, j_{mv} at the same bias condition will be small, since there are few empty states in the semiconductor VB. When a positive bias is applied to the sample (see Figure 7D), j_{cm} will decrease and become negligibly small, since the electrons in the CB of the semiconductor see no empty states in the metal j_{vm} will also be small in the voltage range studied, since the hole concentration in a heavily doped semiconductor is low. j_{mc} will be significant, however, at these positive bias voltages, since E_{FM} is nearly equal to or above the CB of the semiconductor. j_{mc} is expected to increase rapidly with increasing positive bias, since both the surface density of states (SDOS) of the n-FeS_2 sample and the number of electrons in the metal in energy states above the E_{cs} of the semiconductor increase rapidly. Experimentally, we observe a sharp increase of the conductance at positive bias voltage as shown in Figure 5. We also observed some rectifying behavior as shown in Figure 3. This phenomenon might be partly due to the effect of SDOS. As mentioned previously, the current flow in the positive bias region is mainly determined by j_{mc}, and the current flow in the low negative bias region is mainly controlled by j_{cm}. Assuming that the metal has a symmetric DOS distribution or has a constant density of states around E_{FM} and that $k_{mc} = k_{cm}$, the difference in the semiconductor surface electron density (n_s), which determines j_{cm}, and the empty SDOS of the semiconductor, which determines j_{mc}, will produce a difference in j_{cm} and j_{mc}. The n-FeS_2 samples have a surface electron concentration, n_s, of ca. 2.7×10^{18} cm^{-3}, which is nearly independent of the voltage in the low negative-bias region (see the discussion below). The CB DOS of n-FeS_2 has an effective value of 7.5×10^{18} cm^{-3},[14] and the total empty states in the CB of the semiconductor increases with bias voltage. Considering these facts, we think, the above explanation on the rectifying behavior is not unreasonable. However an effect of the electric field enhancement on the electron flow due to the tip curvature, as proposed by Feenstra et al.,[8] might also play a role, since the electric field (or the corresponding potential) is expected to have a strong effect on the electron-transfer rate constant, k. This effect seems much too large to account for the small rectifying behavior we observed here.

From the above discussion, one should expect to obtain a "conductance well" equal to the semiconductor gap, E_g, terminating between two regions of rapidly rising conductance for an ideal MIS tunnel structure. In addition to the four current components associated with the conduction and valence bands of the semiconductor as described above, there may be other currents attributable to semiconductor impurity states (j_{ms} and j_{sm}), for example, impurity bands in degenerate or near-degenerate semiconductors or localized interfacial states. These additional currents may produce features within the normal conductance well that should provide information about the location and density of impurity states. Our experimentally observed conductance and normalized conductance spectra for a near-degenerate n-FeS_2 sample with impurity states as shown in Figures 5 and 6 agree quite well with these predictions.

Gray[15] has suggested that an ideal MIS structure could be useful as a tool for probing the energy band edges (and thus the bandgap) or location of impurity states of a semiconductor, as long as the junction structure is prepared to meet the requirement that the resistance of the space-charge region in the semiconductor is small compared with that of the insulating layer, so that nearly all of the applied bias voltage appears across the insulating layer rather than as band bending in the semiconductor. Thus it is interesting to analyze the voltage drop across the STM gap as a function of applied voltage. For simplicity, we approximate the STM junction with a fairly blunt tip to a one-dimensional MIS structure.

For the following discussion we define the potential at any point in the semiconductor surface region $\psi(x)$, by

$$q\psi(x) = E_{cb} - E_c(x) = E_{vb} - E_v(x) \quad (5)$$

where $x = 0$ indicates the semiconductor/insulator interface. Henceforth subscripts b and s refer to the semiconductor bulk and semiconductor surface, respectively.

When a bias voltage V_a is applied across the MIS structure (see Figure 7D), it divides as it drops across the insulator, ΔV_i, and the semiconductor, $\Delta\psi_s$. Thus

$$V_a = \Delta V_i + \Delta\psi_s \quad (6)$$

The subscript a on any quantity represents its value with applied bias and the subscript 0 with zero bias. ψ_{sa} and ψ_{s0} are the semiconductor surface potential with applied voltage and with zero bias, respectively.

ΔV_i can be expressed in terms of the electric field ϵ_s at the surface of the semiconductor ($x = 0$). Assuming that there is no charge within the insulator, we can apply Gauss' law to a surface with one plane in the insulator and the other just inside the semiconductor at the interface to obtain

$$\epsilon_i \varepsilon_i - \epsilon_s \varepsilon_s = Q_{ss} \quad (7)$$

Here ϵ_i and ϵ_s are the permittivities of the insulator and the semiconductor, respectively, ε_i is the electric field in the insulator, ε_s is the electric field at the semiconductor surface, and Q_{ss} is the charge in surface states. Because we are assuming there is no charge in the insulator

$$V_i = s\varepsilon_i \quad (8)$$

where s is the width of the insulator (i.e., the tip–sample separation). The combination of eqs 7 and 8 gives

$$V_i = (s/\epsilon_i)(\epsilon_s\varepsilon_s + Q_{ss}) \quad (9)$$

Thus

$$\Delta V_i = (s\epsilon_s/\epsilon_i)(\varepsilon_{sa} - \varepsilon_{s0}) + (s/\epsilon_i)(Q_{ssa} - Q_{ss0}) \quad (10)$$

The electric field at the surface of the semiconductor can be obtained by one integration of Poisson's equation as a function of the surface potential[10]

$$\varepsilon_s = \pm(2q/\beta\epsilon_s) \times \{n_b[\exp(\beta\psi_s) - 1 - \beta\psi_s] + p_b[\exp(-\beta\psi_s) - 1 + \beta\psi_s]\}^{1/2} \quad (11)$$

(13) For electron tunneling, $k_{\mu\nu}$ is proportional to the transmission coefficient of the electron. See, for example: (a) Tersoff, J.; Hamann, D. R. *Phys. Rev. Lett.* **1983**, *50*, 1998. (b) Selloni, A.; Carnevali, P.; Tosatti, E.; Chen, C. D. *Phys. Rev. B* **1985**, *31*, 2602. (c) Lang, N. D. *Phys. Rev. B* **1986**, *34*, 5947.

(14) Kou, W. W.; Seehra, M. S. *Phys. Rev. B* **1978**, *18*, 7062.

(15) Gray, P. V. *Phys. Rev. A* **1965**, *140*, 179.

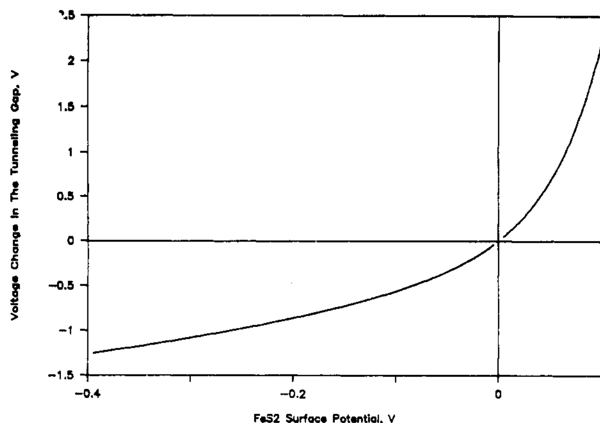

Figure 8. Change in the voltage of the tip–substrate gap as a function of the semiconductor surface potential.

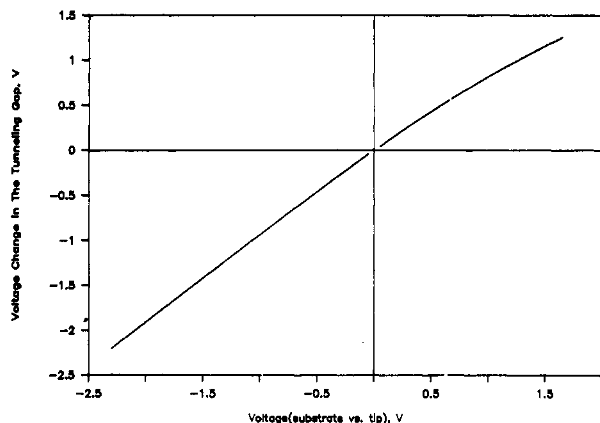

Figure 9. Change in the voltage across the tip–substrate gap as a function of applied bias voltage. The following parameters have been used to obtain Figures 8 and 9. $n_b = 2.7 \times 10^{24}$ m^{-3}; $p_b = 1.8 \times 10^9$ m^{-3}; $\epsilon_s = 10.9\epsilon_0$; $\epsilon_i = \epsilon_0$; $s = 2 \times 10^{-9}$ m; $E_g = 0.95$ eV; $\psi_{s0} = 0$ V; $V_{i0} = 0$ V; $Q_{ssa} = Q_{ss0} = 0$.

Here the + or − sign is chosen based on the sign of ψ_s, $\beta = q/k_BT$, with k_B the Boltzmann constant and T the absolute temperature, n_b and p_b are the electron and hole densities in the bulk of the semiconductor, respectively.

Q_{ss} is also a function of ψ_s. Thus one can express ΔV_i and V_a as functions of ψ_s. We will first discuss the voltage distribution across the structure by assuming no surface states ($Q_{ss} = 0$). Figure 8 is a plot of ΔV_i as a function of ψ_s for $n_b = 2.7 \times 10^{24}$ m^{-3} and $p_b = 1.8 \times 10^9$ m^{-3}, which are the n_b and p_b values of the n-FeS_2 sample used. The plot of ΔV_i as a function of applied voltage is shown in Figure 9.

For the calculations leading to Figures 8 and 9 we have assumed no initial band bending ($\psi_{s0} = 0$ V) and no surface states $Q_{ssa} = Q_{ss0} = 0$ and used the following parameters:

$\epsilon_s = 10.9\epsilon_0$[16] ($\epsilon_0$ is the permittivity of free space)

$$\epsilon_i = \epsilon_0$$

$$s = 2 \times 10^{-9} \text{ m}$$

$E_g = 0.95$ eV (E_g is the bandgap of semiconductor)

$N_c = N_v = 7.5 \times 10^{24}$ m^{-3}[14] (N_c and N_v are the effective DOS at the CB and VB edges of FeS_2, respectively)

For the parameters used above, the upper edge of the conductance well will occur at a bias of ca. 0 V (assuming no initial band bending). The second edge of the conductance well occurs at a voltage in the negative bias region. Since the applied voltage in the negative bias region drops almost entirely (>95%) across the insulating layer, one will expect a conductance well with the width essentially equal to the bandgap of FeS_2. This is what is shown in Figure 6. In the positive bias region, as shown in Figure 9, a small but significant amount of the applied voltage drops across the space charge layer. For example, a bias voltage of 1.5 V will change the magnitude of the semiconductor surface potential by ca. 0.25 V. This band bending will not affect the measurement of the width of the conductance well, since it occurs in the positive bias region while the well is mainly measured in the negative-bias region; however, it will distort somewhat the conductance spectrum in the positive-bias region. Both the distortion of the conductance well and the spreading of the conductance well width, with respect to the energy gap, could become severe when the doping concentration decreases or the thickness of the insulator is too thin. Quantitative analyses of the conductance spectra in these cases will be less straightforward, and they will become even more complicated when high densities of surface states exist in the energy gap.

From eq 10 it can be seen that the change in voltage across the insulator when a bias is applied depends upon the change in the amount of charge in surface states. The width of the conductance well will also depend upon the surface states. We do not intend to do a quantitative analysis of the effect of surface states in this paper but rather give a qualitative picture based on simple physical concepts. One can see that charge in surface states will terminate field lines starting at the metal, so that the semiconductor is more perfectly shielded from the metal the higher is the surface state density. This leads to a smaller change in the semiconductor surface potential with applied voltage, and the width of the conductance well will be narrower than the identical system without surface states. The last term shown in eq 10 actually represents the difference in voltage, δV_i, across the insulator for a given semiconductor surface potential, with and without surface states. Clearly δV_i, and thus the well width, will depend upon the density of surface states and their location (energy).

Concerning the origins of the conductance peaks shown in Figure 6, it is interesting to point out that Li et al.[17] observed in a UPS study a narrow (ca. 0.8 eV wide), localized level just below the VB edge and lying above a broad VB background. Theoretical calculations[17,18] indicate that this level is the Fe 3d-like t_{2g} states and has ca. 85% of its electronic charge in the Fe atomic region and only 4% within the S atomic regions, with the remainder of its charge in the interatomic regions. Thus, the uppermost VB is fairly localized and nonbonding in character. In contrast, the CB contains significant admixtures from other orbitals. For example, the lowest unoccupied e_g band shows considerable S 3p mixing, with 69% and 30% of the charge in the Fe and S regions, respectively, resulting in an antibonding band of width of ca. 1.8 eV. From the energy locations of the conductance peaks observed and the consistency of their shapes and width with the theoretical calculations, we attribute the peak at −1.6 V to electron transfer between the tip and the fairly localized uppermost valence level mainly consisting of Fe 3d t_{2g} states. The broad peak in the positive bias region is attributed to electron transfer between the tip and the broad, delocalized, CB of FeS_2. However, shape distortion and a shift of the peak position caused by "band bending", as discussed above, may be significant in lightly doped samples. One must also consider the possibility that conduction may become limited by transport processes inside the semiconductor for low-conductivity samples, especially when E_{FM} is opposite either of the intrinsic semiconductor bands. Large band bending due to an iR drop in the semiconductor may occur due to a large current flow.

Finally, note that these distinct bias-dependent conductance data qualitatively agree with those bias-dependent current images shown in Figure 2. As suggested by the conductance measurements, the fcc structure formed by the Fe atoms should be resolved at large negative bias voltage (e.g., ≤−1.0 V) while a wavy surface

(16) Husk, D. E.; Seehra, M. S. *Solid State Commun.* **1978**, *27*, 1147.

(17) Li, E. K.; Johnson, H. K.; Eastman, D. E.; Freeouf, J. L. *Phys. Rev. Lett.* **1974**, *32*, 470.

(18) (a) Bullett, D. W. *J. Phys. C* **1982**, *15*, 6163. (b) Lauer, S.; Trautwein, A. X.; Harris, F. E. *Phys. Rev. B* **1984**, *29*, 6774.

structure contributed by both the Fe and the S atoms will be obtained at small negative bias and all positive bias voltages. One might also expect to observe electronic heterogeneity of the surface on a large scale as clearly demonstrated in Figure 1.

Conclusions

We have demonstrated the usefulness of the STM in conjunction with related spectroscopic techniques for studying semiconductor surfaces. The TS technique yields information about the energy-band structure of the semiconductor and about impurity states. STS should also reveal spatial variation of electronic structure over the surface and perhaps various states associated with chemical contamination. We have suggested some problems associated with these measurements and some precautions one has to take in the interpretation of the experimental results. Finally, we should emphasize that the present study and our previous study on n-TiO_2 (001) surface are exploratory ones. We are now investigating the applicability of these techniques to the in situ study of the electrode/electrolyte interface.

Acknowledgment. The support of this research by the Texas Advanced Research Program and NSF (CHE 8805685) is gratefully acknowledged. We are indebted to Dr. Helmut Tributsch for his contribution of the samples of FeS_2.

Electron Donor–Acceptor Orbital Correlations. 8. Selection Rules for Vibrational Enhancement of Intermolecular Electron Transfer

William A. Glauser, Douglas J. Raber, and Brian Stevens*

Department of Chemistry, University of South Florida, Tampa, Florida 33620 *(Received: June 18, 1990)*

Transient intermolecular vibrational modes of the intermediate 1:1 donor–acceptor complex not only permit energy conservation along the reaction coordinate but by virtue of their transformation properties also modify the symmetry of the reaction surfaces involved in intermolecular electron transfer. Symmetry species are assigned to these transient modes for complexes belonging to C_s, C_{2v}, and C_{3v} point groups in order to identify those modes that provide an adiabatic channel for the electronically diabatic process. Since each symmetry species of these point groups is represented by at least one transient mode, it is concluded that geminate charge recombination via unconstrained 1:1 EDA complexes should be efficient.

Introduction

In common with other chemical and photochemical processes, intermolecular electron transfer is usually defined in exclusive electronic terms, and its reaction coordinate is described with reference to Born–Oppenheimer (nuclear potential energy) surfaces. In this context the transfer of an electron from electronically excited donor D* to acceptor A in sequence 1 may be classified

$$D^* + A \rightarrow (D^*A) \rightarrow (D^+A^-) \rightarrow D^+ + A^- \quad (1)$$

as adiabatic if zeroth-order locally excited (LE) and charge-transfer (CT) configurations $|D^*A\rangle$ and $|D^+A^-\rangle$ belong to the same symmetry species of the point group describing the intermediate complex, or as diabatic if it involves a nonradiative transition $(D^*A) \rightarrow (D^+A^-)$ between surfaces of different symmetry[1] (and/or spin angular momentum). In the former case the rate constant increases (within limits) with the free energy separation of LE and CT states,[2,3] whereas the rate constant of a diabatic process increases[4,5] as this energy gap is reduced; accordingly the efficient production of radical ion pairs of high redox potential (and minimum energy loss) is promoted by diabatic electron transfer.[6]

If Γ_1 denotes the totally symmetric representation of the D/A complex point group, the adiabatic requirement is expressed by condition 2a, which, in terms of symmetry species of donor (ϕ_{-2}

$$\Gamma(|D^*A\rangle) \otimes \Gamma(|D^+A^-\rangle) = \Gamma_1 \quad (2a)$$

$< \phi_{-1} < \phi_1^* < \phi_2^*$) and acceptor ($\theta_{-2} < \theta_{-1} < \theta_1^* < \theta_2^*$) frontier orbitals (subjuced to the same point group) reduces[6] to condition 2b if D* has the electron configuration $\phi_{-2}{}^2\phi_{-1}\phi_1^*$. Condition 2

$$\Gamma(\phi_1^*) \otimes \Gamma(\theta_1^*) = \Gamma_1 \quad (2b)$$

also describes "strong" exciplex formation insofar as $\Gamma(|D^+A^-\rangle) = \Gamma(|D^*A\rangle \neq \Gamma_1$ and the CT configuration $|D^+A^-\rangle$ cannot interact with the Γ_1 ground state.

In this way selection rules proposed[6] for adiabatic intermolecular electron transfer between various (^1L_a, ^1L_b) donor and acceptor states have been formulated in terms of the intermediate complex description as either a ("strong" or "weak") exciplex or EDA complex. Thus the condition

$$\Gamma(|D^*A\rangle) \neq \Gamma(|D^+A^-\rangle) = \Gamma(|DA\rangle) = \Gamma_1 \quad (3)$$

defines diabatic electron transfer, "strong" EDA complex formation, and (efficient) adiabatic exoergic charge recombination (process 4), and it has been proposed that "weak" EDA complexes

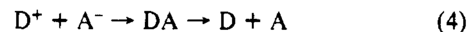

$$D^+ + A^- \rightarrow DA \rightarrow D + A \quad (4)$$

associated with diabatic charge separation and diabatic charge neutralization offer the most efficient photochemical source of *separated* radical ions of high redox potential.[6]

Insofar as the overall energy E_r of a *reacting* system is conserved, this must undergo a continuous redistribution between nuclear and electronic terms as the reaction proceeds. This is illustrated in Figure 1 for activated (Figure 1a) and activationless (Figure 1b) processes where nuclear kinetic energy curves $T_n(q)$ appear as mirror images of potential (Born–Oppenheimer) energy curves $E_{BO}(q) = (V_n + T_e + V_e)(q)$ about E_r; here the nuclear kinetic energy of reactants supplies the activation energy where necessary (Figure 1a) whereas that of the products accommodates both the activation energy and the internal energy change ΔE_{BO}. Since the translational and rotational contributions to nuclear kinetic energy have no potential energy component, the partitioning of E_r between T_n and E_{BO} along the reaction coordinate must be described in terms of nuclear displacements that transform as

(1) Forster, Th. *Pure Appl. Chem.* **1970**, *24*, 443.
(2) Marcus, R. A. *Ann. Rev. Phys. Chem.* **1964**, *15*, 155.
(3) Rehm, D.; Weller, A. *Isr. J. Chem.* **1970**, *8*, 259.
(4) Robinson, G. W.; Frosch, R. P. *J. Chem. Phys.* **1963**, *38*, 1187.
(5) Siebrand, W. *J. Chem. Phys.* **1967**, *46*, 440.
(6) Stevens, B. *Chem. Phys.* **1988**, *122*, 347.

0022-3654/91/2095-1976$02.50/0 © 1991 American Chemical Society